Journal of Materials Research and Technology 37 (2025) 3739–3751

Contents lists available at ScienceDirect

Journal of Materials Research and Technology

journal homepage: www.elsevier.com/locate/jmrt

The impact of sintering and Mg doping on the ionic conductivity of $Sm_2Zr_2O_7$ pyrochlores

Silvia Blasco-Zarzoso [a,*], Emerson Luiz dos Santos-Veiga [c], U-Chan Chung [b], Sebastien Fourcade [b], Catherine Elissalde [b], Fabrice Mauvy [b], Eloísa Cordoncillo [a,**], Hector Beltrán-Mir [a,***]

[a] Departamento de Química Inorgánica y Orgánica, Universitat Jaume I, Castellón de la Plana, 12071, Spain
[b] CNRS, Université de Bordeaux, ICMCB, 87 avenue du Dr. A. Schweitzer, Pessac, F-33608, France
[c] Energy and Nuclear Research Institute (IPEN-CNEN), 05508-000 São Paulo, SP, Brazil

ARTICLE INFO

Keywords:
Spark plasma sintering
Pyrochlore
Ionic conductivity
Electrochemical impedance spectroscopy

ABSTRACT

Pyrochlore structures based on $Sm_2Zr_{2-x}Mg_xO_{7-x}$ (x = 0, 0.1, 0.15 and 0.2) were synthesized by hydrothermal method at 180 °C and the resulting powders fired at 1200 °C for 2h. Two sintering methods were employed: Conventional Sintering (CS) with uniaxial pressing and Spark Plasma Sintering (SPS), both at 1350 °C. Resulting pellets had relative densities of ~70 % (CS) and ~97 % (SPS), with nano-size grains.

Electrochemical Impedance Spectroscopy (EIS) was performed under various atmospheres to assess the impact of sintering on electrical properties. All samples exhibit ionic conductivity, with Mg-doped compositions showing the highest conductivity whatever the sintering process used. SPS samples showed higher conductivity than those sintered by CS, with the x = 0.10 composition (SMZ01) exhibiting the highest conductivity. The overall conductivity was unaffected by atmosphere (air, N_2 and H_2–N_2), indicating good stability and resistance to reduction/oxidation. Notably, SMZ01 sintered by SPS exhibits total conductivity comparable to Yttria-Stabilized Zirconia (YSZ), a standard electrolyte in oxide-ion conducting applications. These Mg-doped ceramics, especially when processed by SPS, offer excellent relative density and conductivity, making them promising candidates for use in Solid Oxide Fuel Cells (SOFCs), Solid Oxide Electrolysis Cells (SOECs), gas sensors, and other clean energy technologies requiring thermal and physical stability.

1. Introduction

In recent decades, research has intensified to find alternatives to current energy sources that are more economical and, above all, non-polluting. Although nuclear and fossil sources remain the primary energy providers, environmental awareness and the limitation of current resources, such as oil and coal, make it essential to find new ways of generating, storing, and distributing energy.

The most significant advances in this field are oriented towards technologies that harness renewable energy sources, such as solar cells and fuel cells. These technologies, in turn, require efficient energy storage methods, making the field of rechargeable batteries one of most actively researched topics today.

The increased use of battery-powered portable electronic devices, along with the development and growing interest in low or zero-emission vehicles, has made ionic conductors a central focus of these developments. Consequently, these materials play a fundamental role in modern technology and remain the subject of ongoing research and development aimed at discovering new applications and improvements in their properties.

Ceramic materials with high ionic conductivity are used, for example, in Solid Oxide Fuel Cells (SOFCs) and Solid Oxide Electrolysis Cells (SOECs). In SOFC technology, fuel oxidation occurs at the anode, releasing electrons, while O^{2-} ions travel through the electrolyte from the cathode to the anode, where they react with the fuel to complete the electrochemical reaction [1–4]. Ensuring a steady and fast transport of oxygen ions at the electrolyte-electrode interfaces is crucial for achieving optimal cell performance, which in turn requires

* Corresponding author.
** Corresponding author.
*** Corresponding author.
E-mail addresses: blascos@uji.es (S. Blasco-Zarzoso), cordonci@uji.es (E. Cordoncillo), mir@uji.es (H. Beltrán-Mir).

https://doi.org/10.1016/j.jmrt.2025.07.080
Received 28 April 2025; Received in revised form 7 July 2025; Accepted 8 July 2025
Available online 9 July 2025

compatibility and precise control of all cell components.

Pyrochlore-type compounds have been identified as promising oxygen electrode because of the presence of oxygen vacancies in lattice. Pyrochlore materials, with general formula $A_2B_2O_7$, offer interesting flexibility in terms of crystallo-chemistry. The A-site is typically occupied by rare earth cations positioned at the centre of the oxygen octahedra, while the B-site is usually occupied by smaller transition metal cations, which often exhibit higher oxidation states. Additionally, these materials possess inherent anion vacancies at the 8a site, which reside in the tetrahedral interstice between adjacent B-site cations. This distinctive structural arrangement distinguishes pyrochlores as a ceramic class with exceptional chemical and physical properties, along with excellent thermal and chemical stability, making them promising candidates for a wide range of applications [5,6]. The different coordination environments in the pyrochlore structure allows for a diverse cationic arrangements and various oxidation states [7–9].

Thanks to the properties mentioned above, the pyrochlores structures are highly suitable for use in high-temperature applications, including Solid Oxide Fuel Cells [10–13], gas sensors [14–16], and catalytic converters [17,18]. Their effectiveness is particularly notable when incorporating ions with different oxidation states, such as Pr (III/IV) and Ce(III/IV) [19–22]. Moreover, characteristics such as low thermal conductivity [23,24], low dielectric losses [25,26], and ionic conductivity [27–29] make pyrochlore ceramics as strong candidates for advanced energy conversion and storage applications. Among the possible pyrochlore compositions, this work focuses on $Sm_2Zr_2O_7$, including compositions in which different amounts of Zr(IV) is replaced by Mg(II), selected to study its electrical properties.

Table 1 reports a literature survey and summarizes different studies carried out on materials based on $Sm_2Zr_2O_7$ [30–41], including the nominal compositions used and, in each case, the proposed application. Different compositions with various ion dopants substituting Sm or Zr, as well as the stoichiometric composition, have been prepared. Diverse applications are proposed depending on the composition, although their use in SOFCs remains one of the most prominent. The examples cited in Table 1 regarding ceramics used as oxide ionic conductors in applications like SOFCs [30,32–36,40] exhibit high conductivities, comparable with other ionic conductors, which range from 1 to 4.7×10^{-3} S cm^{-1} at temperatures above 800 °C in pellets sintered at 1600–1700 °C. The common synthesis methods used in literature to prepare the powders are solid-state reaction or mechanical activation. Conventional sintering, used either alone or in combination with other sintering methods at different pressures, was employed to prepare the pellets. In some cases, the sintering process involved multiple steps, such as uniaxial pressing at 20 MPa followed by cold isostatic pressing and occasionally concluded with pressureless sintering [33–35]. These studies demonstrate that the synthesis methodology, sintering temperature, and operating conditions used for electrical measurements are key factors in determining the conducting material's properties.

Achieving the desired properties in ceramic materials, particularly pyrochlores, requires careful attention to the processing steps, ensuring the preservation of the crystalline structure while obtaining a dense ceramic. Conventional sintering methods often fall short of achieving the required density (≥95 %) [42]. However, innovative sintering techniques such as Flash Sintering [43], Cold Sintering Process [44], and Spark Plasma Sintering (SPS) [45] have proven highly effective for densifying functional ceramics. Among these, SPS stands out due to its combination of uniaxial pressure and pulsed electrical current, enabling efficient heat transfer and fast sintering kinetics [46–49]. This process significantly improves relative density, enhancing key properties like mechanical strength, electrical conductivity, and chemical stability in pyrochlore ceramics. Additionally, the low partial pressure of O_2 during SPS processing may facilitate the reduction of chemical species, thereby modifying the material's characteristics and increasing their suitability for various applications. Moreover, in terms of energy consumption, low sintering temperature, short cycle, fast heating rates contribute also to the benefits of SPS compared to conventional sintering.

In this context, the present work studies the influence of Mg doping and the sintering process of the powders on the electrical properties of the pyrochlore material with general formula $Sm_2Zr_{2-x}Mg_xO_{7-x}$ (x = 0, 0.1, 0.15 and 0.2) To do so, two different sintering processes were used: Conventional Sintering (CS) and Spark Plasma Sintering (SPS). This work aims to achieve a better understanding of how doping and sintering affect pyrochlore ceramics, thereby advancing our knowledge and broadening the potential applications of these materials.

Table 1
Literature for different compositions based on $Sm_2Zr_2O_7$.

Year	First author	Composition	Application	Ref.
2007	Shlyakhtina	$Sm_2Zr_2O_7$	SOFC	[30]
2008	H.-S. Zhang	$Sm_2(Zr_{0.7}Ce_{0.3})_2O_7$	Thermal conductor	[31]
2009	X.-L. Xia	$(Sm_{1-x}Ca_x)_2Zr_2O_{7-x}$	SOFC	[32]
2011	Z.-G. Liu	$Sm_{2-x}La_xZr_2O_7$	SOFC	[33]
2011	Z.-G. Liu	$(Sm_{1-x-y}Gd_xYb_y)_2Zr_2O_7$	SOFC	[34]
2012	X.-L. Xia	$Sm_{2-x}Eu_xZr_2O_7$	SOFC	[35]
2014	D.S. Vaisakhan	$Sm_2(Zr_{1-x}Ce_x)_2O_7$	SOFC	[36]
2016	Y.-H. Ma	$Sm_2(Zr_{1-x}Ti_x)_2O_7$	Thermo-Optic	[37]
2017	D.Y. Wang	$Sm_2Zr_2O_7$	Thermal barrier	[38]
2018	Wei Guo	$Sm_2Zr_2O_7$	Thermal barrier	[39]
2019	Shlyakhtina	$Sm_{2-x}Ca_xZr_2O_{7-x/2}$	PC-SOFC	[40]
2020	Yong Zheng	$Sm_2Zr_2O_7$	NO_2 detection	[41]

2. Experimental section

2.1. Synthesis of the samples by hydrothermal method

Four compositions based on $Sm_2Zr_{2-x}Mg_xO_{7-x}$ with x = 0, 0.1, 0.15 and 0.2 (named as SZ, SZM01, SZM015 and SZM02, respectively) were prepared using the hydrothermal method. This synthesis method offers advantages over the conventional solid-state method. For example, its ability to produce nano-sized particles, is straightforward and cost-effective, ensures better control of reaction stoichiometry, and is consistently reproducible [21].

The starting reagents were $Sm(NO_3)_3{\cdot}6H_2O$ (99.9 %, Sigma-Aldrich), $ZrOCl_2{\cdot}8H_2O$ (98 %, Sigma-Aldrich) and $Mg(CH_3COO)_2{\cdot}4H_2O$ (98 %, Panreac). Initially, the stoichiometric amounts of each precursor were dissolved in 40 mL of distilled water. The pH of the solution was adjusted to 10 using an ammonium solution (32 % w/w, Scharlab) and was stirred for 10 min. The prepared mixture was placed into a 100 mL Teflon-lined vessel, which was then introduced in a digestion bomb and subjected to heat treatment in an oven at 180 °C for 24 h. The resulting precipitate was cooled and dried at 100 °C for 24 h. Finally, the dried powders were ground and calcined at 1200 °C for 2 h, with a heating rate of 5 °C min^{-1}. A schematic representation of this procedure is shown in Fig. 1 (a).

To perform electrical measurements and investigate the effect of ceramic density on the electrical response, the powders of the undoped and doped samples were pressed and sintered using two different methods: the Conventional Sintering (CS) and the Spark Plasma Sintering (SPS).

2.2. Pellet preparation with conventional sintering (CS) process

The conventional sintering method involved uniaxially pressing the powder into a pellet, with a diameter of 5 mm and a thickness of approximately 1 mm. A force of 1 ton (500 MPa) was applied and maintained for 2 min. After realising the pressure, the pellet was sintered at 1350 °C for 2 h in air with a heating rate of 5 °C min^{-1}. A scheme of this process is shown in Fig. 1(b).

2.3. Pellet preparation with SPS process

Pellets with a diameter of 10 mm and a thickness of approximately 1

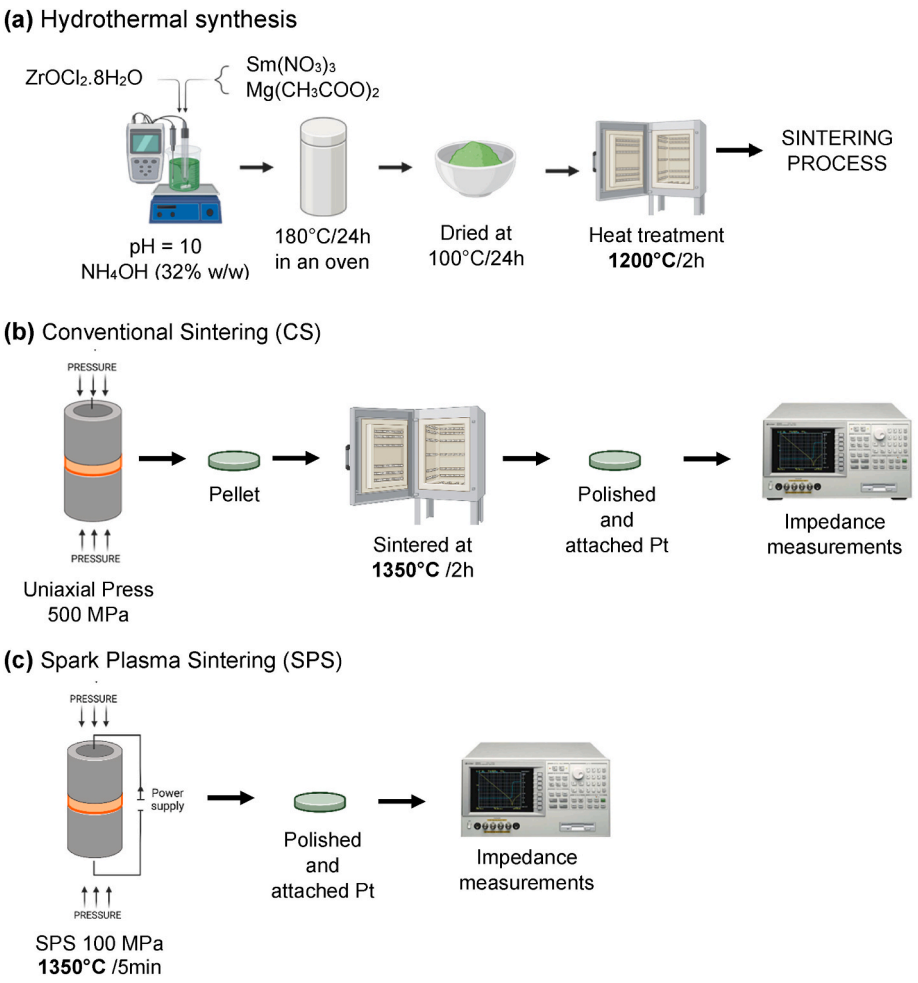

Fig. 1. Schematic representation of (a) hydrothermal synthesis method, (b) Conventional Sintering (CS) process and (c) Spark Plasma Sintering (SPS) process.

mm were prepared from the powders of the samples using SPS. The SPS process was performed using SYNTEX, Dr. Sinter Lab model 515S equipment as schematically depicted in Fig. 1(c). To prevent graphite oxidation, the process was carried out under a primary vacuum (≈10 Pa) at a temperature of 1350 °C. A short dwell time of 5 min and high heating rates (50 °C–100 °C min^{-1}) were employed to enhance densification while minimizing grain growth. A uniaxial pressure of 100 MPa was applied from room temperature and maintained throughout the heating process until the sintering time at the target temperature was completed. During the cooling step, the pressure was gradually released when the temperature dropped to T ≤ 600 °C. Then, the current was switched off and the sample was allowed to cool at room temperature. Graphite molds and punches were used in the process, with the interior of the mold covered with graphite foil to ensure optimal electrical contact between all components.

For both CS and SPS prepared samples, the final pellets were polished to clean the surface before depositing the platinum electrodes to carry out the electrical measurements.

2.4. Characterization techniques

Phase analysis of the samples was carried out using powder X-ray diffraction (XRD) with a Bruker-AXS D8 X-ray diffractometer with CuK_α radiation. Measurements were conducted at room temperature over a °2θ range of 10°–70°, using a step size of 0.03° and a counting time of 1 s per step.

The experimental density of the sintered pellets was measured through the Archimedes method [50], with several repetitions performed for each sample to ensure data accuracy and reproducibility. Relative density and densification percentages were calculated by comparing the theoretical density obtained from XRD and the experimental density.

Raman spectra of the different compositions were recorded in the frequency range of 200–700 cm^{-1} at room temperature using a modular Raman system (WITec GmbH). The system features an automatic vertical confocal microscope (alpha300 apyron), an ultra-high-efficiency EMCCD detector cooled to 60 °C, and a 532 nm laser coupled to the microscope.

The morphology and microstructure of the pellets were analyzed using a JEOL 7001F Field-Emission Scanning Electron Microscope (FE-SEM) equipped with an energy dispersive X-ray Spectrometer (EDX) from Oxford instruments, using an acceleration voltage of 15 kV. For the analysis, a cross section of the pellets was used. The samples were placed on carbon supports and coated with sputtered platinum.

Electrochemical Impedance Spectroscopy (EIS) using an impedance analyzer (Agilent 4294A, Madrid, Spain) was used to study the electrical behavior of the prepared materials. Both faces of the pellets were coated with platinum paste electrodes, which were dried and decomposed by gradual heating to 800 °C. The electrode-coated samples were placed in a conductivity jig and placed within a quartz chamber to enable and control the gas flow. EIS measurements were performed using an AC voltage of 0.1 V in a frequency range from 40 Hz to 13 MHz. Measurements were conducted at different temperatures, ranging from room temperature to 800 °C, and under various atmospheres, including dry N_2, O_2 and a mixture of 5 %H_2 - 95 %N_2. Impedance data were corrected according to the geometric factor of the pellets.

3. Results and discussion

3.1. Structural and morphological evaluation

XRD patterns of the powders obtained after hydrothermal synthesis and fired at 1200 °C for all compositions revealed a single-phase ordered pyrochlore structure (*Fd-3m* space group) for all samples, Fig. S1 of the Supplementary Information. Pellets prepared using both CS and SPS at 1350 °C were also analyzed by XRD, confirming that the pyrochlore structure is maintained for all compositions and whatever the sintering process, Fig. 2a and b. The formation of the ordered pyrochlore phase is evidenced by the appearance of superstructure peaks around $2\theta \approx 14^{\circ}$ (111) and 37° (331), as indicated by the *hkl* planes in these figures. These peaks arise from the structural reorganization required to convert a fluorite phase into a pyrochlore. This transformation involves scattering effects caused by the rearrangement of A- and B-site cations, the displacement of oxygen atoms from their ideal lattice positions, and the introduction of oxygen vacancies [51,52]. In cases where these superstructure reflections are less evident, Raman spectroscopy (discussed later) will provide additional confirmation of the XRD observations.

No peak displacement toward higher 2θ angles was observed, as might be expected when an ion of a different size replaces another according to Bragg's Law, $n\lambda = 2d\cos\theta$. This is consistent with the similar ionic ratios of Zr(IV) and Mg(II) for the same coordination index [53]. Moreover, no appreciable peak of MgO or other additional phases can be observed, which could indicate that the solid solution is formed.

The XRD patterns also clearly reveal broader peaks in the SPS samples compared to the CS samples, which would likely indicate a reduction in crystallite size in the SPS samples. The commonly accepted formula for calculating the average crystallite size of a material based on the broadening of XRD peaks is known as the Scherrer formula [54], equation (1):

$$t = \frac{K\lambda}{B\cos\theta_B} \tag{1}$$

where, t is the thickness of the crystals (in Å), λ the X-Ray wavelength, θ_B is the Bragg diffraction angle, *K* is the dimensionless factor that depends of the shape of the crystallites in the powder (commonly assigned a value of 0.9), and B is the FWHM (Full Width at Half Maximum) of the XRD peak at the diffraction angle, Table 2. The average crystallite size for powder samples was around 87 nm, whereas for the samples prepared by CS and SPS was 108 nm and 93 nm, respectively. It is clear that the sintering method affects the final crystallite size and that SPS allows limiting grain growth.

In order to confirm that the pyrochlore structure was obtained in all the samples prepared by both sintering methods at 1350 °C, complementary analyses were performed using Raman spectroscopy. According to factor group analysis, $A_2B_2O_7$ pyrochlores are expected to exhibit six Raman-active and seven infrared-active vibrational modes, that in the case of Raman can be represented as follows:

$$\Gamma = A_{1g} + E_g + 4F_{2g} \tag{2}$$

The ordered pyrochlore structure has six active Raman modes, while the defective fluorite structure has only one mode, F_{2g}. The Raman spectra of the samples prepared by both sintering methods have similar profiles, Fig. 3(a) and b. The five active modes identified in the range of 200–700 cm^{-1} are marked in each spectrum. As reported in the literature [55,56], the Raman band at.

525 cm^{-1}, known to exhibit notable intensity variations under different polarization directions, is assigned to the A_{1g} mode (BO_6 bending vibrations). The most intense peak, corresponding to the E_g mode at approximately 302 cm^{-1}, is primarily attributed to the O–B–O bending vibrations, whereas the other two vibration frequencies at ~390 and 599 cm^{-1}, can be assigned to two of the four F_{2g} modes and occurs mainly due to B–O stretching, with contributions from A-O

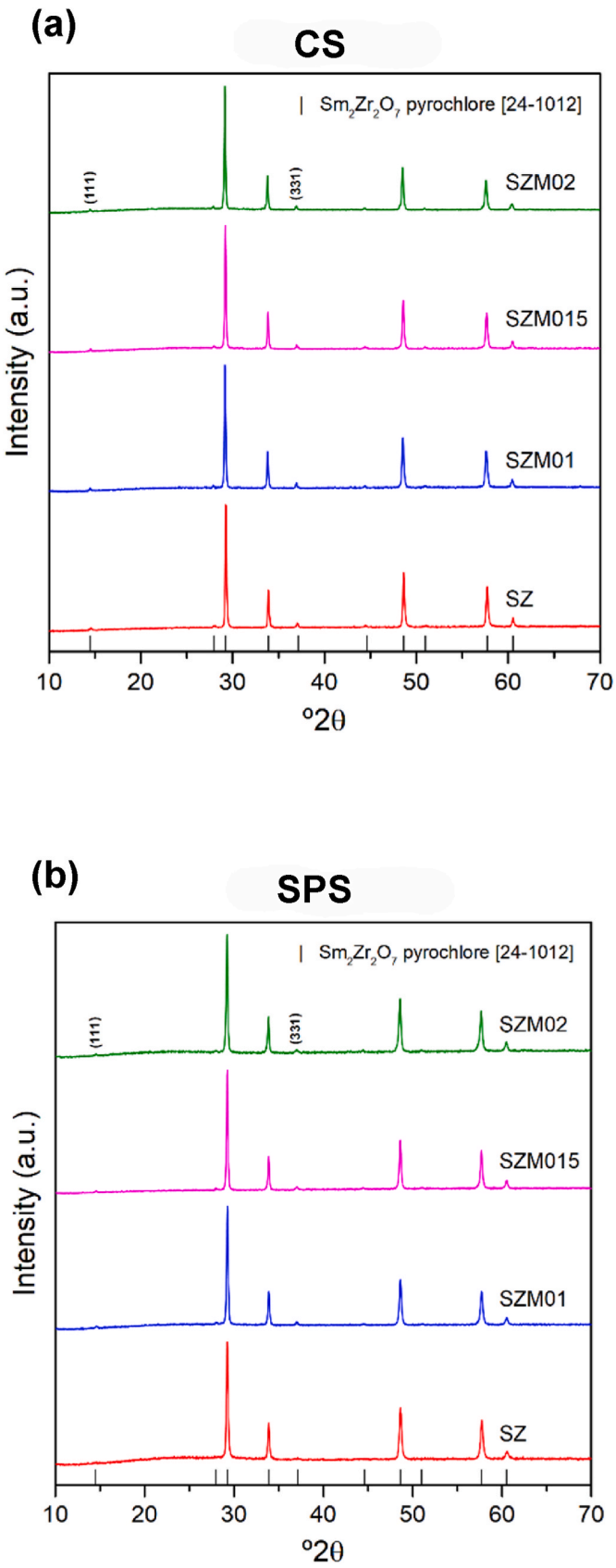

Fig. 2. XRD patterns of the pellets prepared by (a) CS and (b) SPS process, both sintered at 1350 °C for 2h. The reference phase for $Sm_2Zr_2O_7$ (JCPDS – ICDD 24–1012) is included.

Table 2
Average crystallite size and relative densities of the powder and pellets sintered using CS and SPS. Apparent densities were calculated by Archimedes Method.

	SZ	SZM01	SZM015	SZM02
Powder (1200 °C)				
Crystallite size/nm	72(4)	94(5)	92(5)	90(5)
Conventional sintering (CS)				
Crystallite size/nm	104(5)	108(5)	111(6)	107(5)
Apparent density/g cm^{-3}	4.6131	4.6204	4.5918	4.6889
Relative density/%	68	70	70	72
SPS				
Crystallite size/nm	80(4)	98(5)	99(5)	95(5)
Apparent density/g cm^{-3}	5.9691	6.4100	6.3851	6.2006
Relative density/%	93	97	98	96

stretching and O–B–O bending vibrations. A much weaker peak, observed at ~474 cm^{-1}, appears most prominent in samples prepared by conventional sintering, and may correspond to another F_{2g} mode. The reduction or absence of this band, associated with the vibrational modes of the Zr–O bond in the octahedral environment (ZrO_6), could indicate a higher degree of disorder in the structure, and consequently, an increased number of oxygen vacancies [57]. This could be the case in samples prepared by SPS, where higher disorder and a greater number of defects may be present.

Therefore, the results obtained by Raman corroborate the XRD findings and indicate the presence of a pyrochlore phase in all samples prepared using both sintering methods. In addition, based on Raman spectra, the samples prepared by SPS could have a greater number of oxygen vacancies resulting in structural disorder, which may affect the electrical properties of the material.

The relative density of each pellet was calculated by comparing the experimental density, determined using Archimedes' principle, with the theoretical density. The results, summarized in Table 2, indicate that pellets prepared by the CS method at 1350 °C for 2 h achieved relative densities around 70 %, whereas pellets prepared by SPS reached relative densities of around 97 % for Mg doped ones. This demonstrates that the combined effect of pressure and the rapid heating employed in SPS significantly enhances densification, emphasizing the high efficiency of SPS in producing dense ceramics within significantly short sintering times. It is important to note that magnesium also slightly improved densification, in particular for conventional sintering.

Fig. 4 shows the SEM micrographs of cross section of the pellets prepared using CS and SPS, highlighting the distinct microstructural features in the two compositions, SZ and SZM01. Note that the samples doped with higher Mg content had similar microstructure than the composition SZM01, and therefore, were not included in this figure. In view of the grain size revealed by SEM, polycrystalline grains are considered, and the samples prepared by CS exhibit larger grain sizes than those prepared by SPS. However, it is challenging to estimate the average grain size due to the high level of densification. Note that transgranular fracture mode is observed in Mg-doped samples prepared by SPS, reflecting a strengthening of the grain boundaries. This improvement in density, increasing it, and reduction in grain size of the samples prepared by SPS could significantly enhance the electrical properties, particularly the transport of oxide ions [58–60], and also offers advantages, such as the improvement of mechanical properties. There was no evidence of secondary phases by backscattered electron analysis and EDX for all compositions.

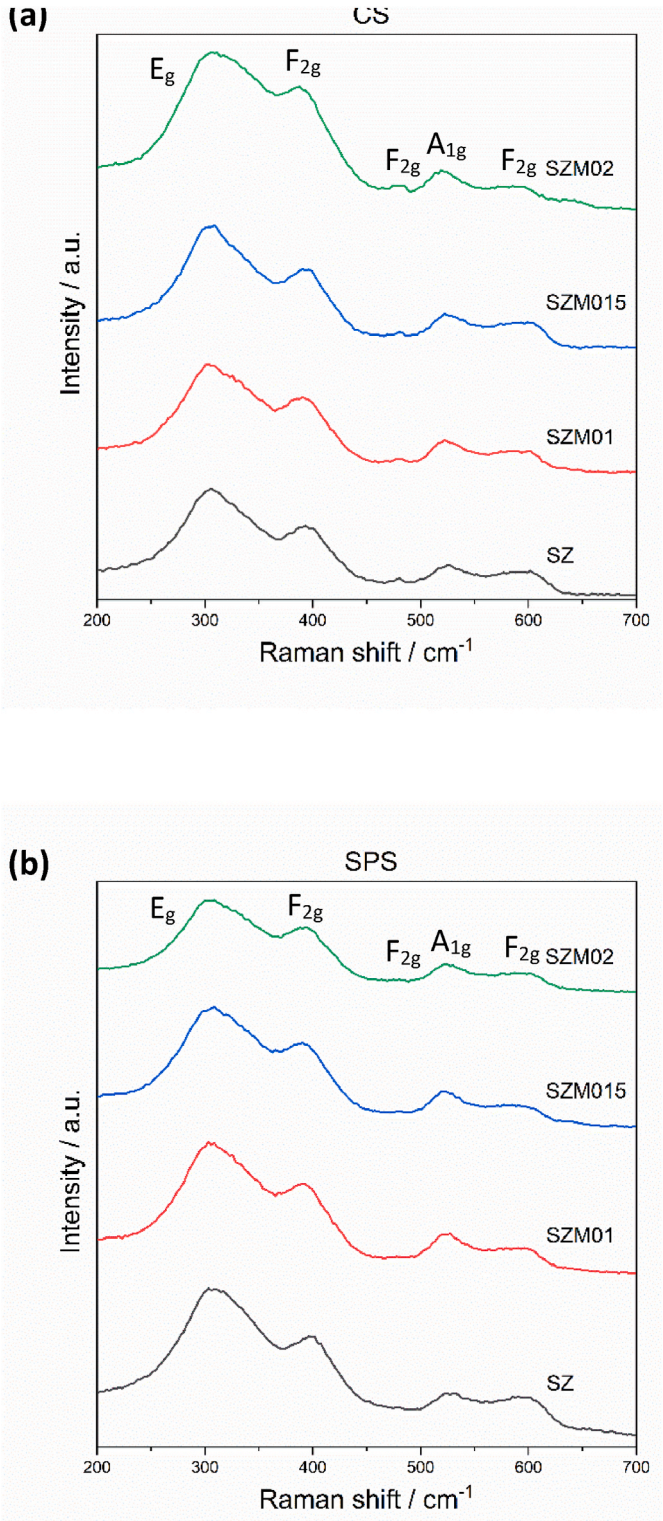

Fig. 3. Raman spectra of the pellets prepared by (a) CS and (b) SPS process, both sintered at 1350 °C for 2h.

3.2. Electrical measurements under nitrogen

Although the low partial oxygen pressure generated during the SPS process could cause partial reduction of the materials during sintering, in this case, as confirmed by ref. [61], and as will show later, these samples, due to their constituent elements, do not undergo any reduction. Nevertheless, to prevent any changes in the oxygen content that could affect the results of the electrical measurements, these were carried out under a dry nitrogen atmosphere.

EIS measurements were used to characterize the electrical behaviour of ceramics. EIS is a powerful tool to determine the ionic conductivity of the ceramic sample but could also help to distinguish the bulk and grain boundaries contributions. Such analysis is very important because ionic conductivity of polycrystalline ceramic is influenced by the sample

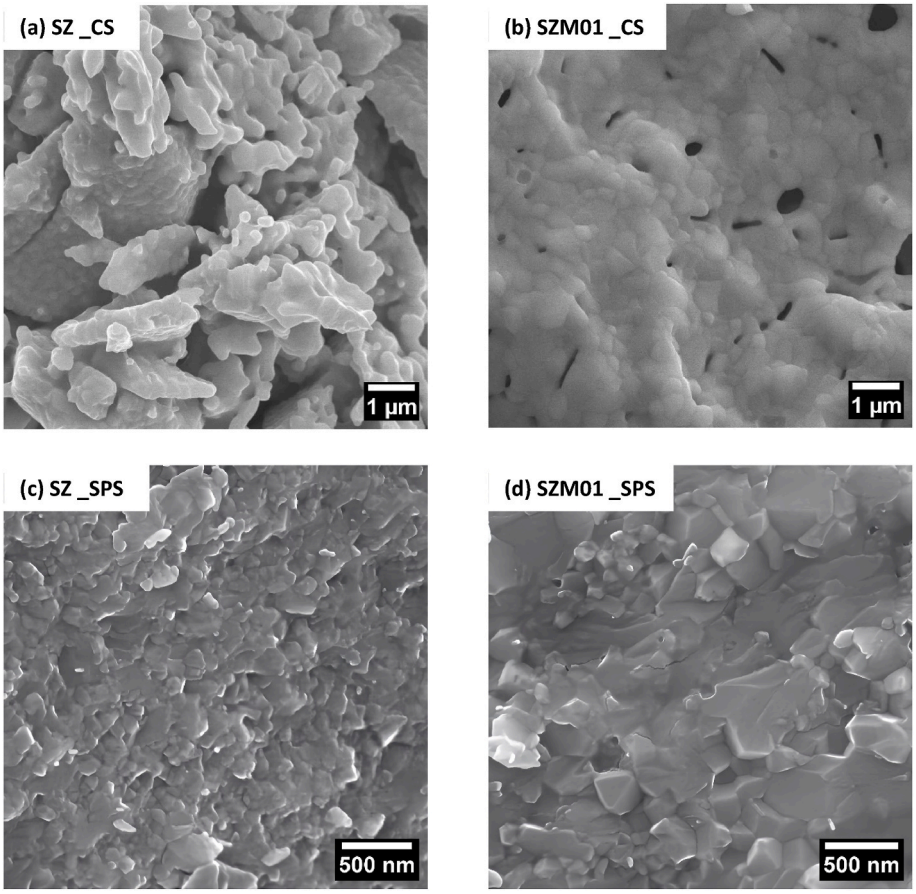

Fig. 4. Micrographs of the cross section of the pellets sintered at 1350 °C by CS and SPS for: (a–b) SZ and (c–d) SZM01.

microstructure. A selection of typical impedance data for two of the four compositions prepared, undoped (SZ) and a Mg doped sample (SZM01) sintered by the two methodologies proposed, CS and SPS, at 1350 °C, is shown in Figs. 5 and 6. Note that the other Mg doped samples with higher concentration are not included for the analysis because they presented similar electrical behavior to SZM01 (Fig. S2 of the Supplementary Information).

Fig. 5(a) and (b) present the impedance complex plane plots, Z*, also referred as Nyquist plots (-In(Z) *versus* Re*(Z), -Z″ versus Z'*), at 450 °C and 650 °C for the undoped sample (SZ) sintered by the two procedures, a broad and distorted semi-circular arc is observed in both samples, indicating the presence of multiple RC (resistance-capacitance) elements connected in series. The total resistivity, $R_1 + R_2$, of the sample prepared by CS is higher than that prepared by SPS. The resistivity values, obtained from the intercept of the arc on the Z' axis, are around 150×10^3 Ω cm for the CS sample and 75×10^3 Ω cm for the SPS sample at 450 °C. This clearly demonstrates the effect of the sintering procedure on the electrical response of the samples.

Z"/M″ spectroscopic plots are widely recognized as effective tools for distinguishing the various contributions to the overall electrical response, particularly when the separation of different regions within a sample is unclear in the complex impedance (Z) plots. Therefore, to better identify the possible presence of two distinct impedance contributions in these samples, Z″/M″ spectroscopic plots for the SZ composition prepared by both the two sintering processes, are shown in Fig. 5 (c) and (d). As can be seen, the peak maxima of M″ and Z″ do not match at the same frequency. The largest peak in the M″ plot is associated with the region of the sample exhibiting the lowest capacitance, corresponding to the sample grains [62]. This M″ peak coincides with the high-frequency peak or shoulder in the Z" plots, indicating that R_1 corresponds to the bulk resistance of the samples. Note that, the Z″ peak in both diagrams displays a broader shape than what is expected for an ideal Debye peak. Therefore, for both samples, the impedance data may be represented ideally by an equivalent circuit containing two parallel RC elements in series. This electrical inhomogeneity within the sample becomes more pronounced as the degree of sintering increases.

Capacitance values can be determined from the maxima in Z"/M" plots, using the relation: $2\pi f \cdot R \cdot C = 1$, however, they are more directly observed in capacitance, C', versus frequency plots, as shown for the same data in Fig. 5(e) and (f). All measurements show a high-frequency plateau at $\sim 5 \times 10^{-12}$ F cm^{-1} which represents the bulk capacitance, C_1, of the samples, and a less well-resolved and low-frequency plateau, C_2, at $\sim 2–3 \times 10^{-11}$ F cm^{-1}. Although the capacitance value, C_2, is lower than typically expected for a grain boundary or surface layer, it still corresponds to an additional R_2C_2 element associated with a small volume fraction resistance. This inhomogeneity may result from grain boundary constriction and/or an inhomogeneous distribution of the ions within the sample.

At low frequencies and high temperatures, C' increases reaching values ranging from approximately 10^{-7} to 10^{-6} F cm^{-1}, depending on the sintering process. These values are characteristic of ion blocking at a sample-electrode interface. At high temperatures, low-frequency ionic conductors typically exhibit capacitance values exceeding 10^{-6} F cm^{-1} [63]. This behavior is also reflected in the characteristic spike or a small semicircle, with a small resistance associated, observed at low frequencies in the impedance complex plane plots. Therefore, these results confirmed that the ionic conduction mechanism due to O^{2-} ions is prevailing in the transport properties.

For the Mg-doped samples, the EIS measurements for both sintering processes were similar to those of the undoped sample. A selection of impedance data for the sample with $x = 0.1$ is shown as an example in Fig. 6(a) and (b) for the two sintering processes. Two distinct RC

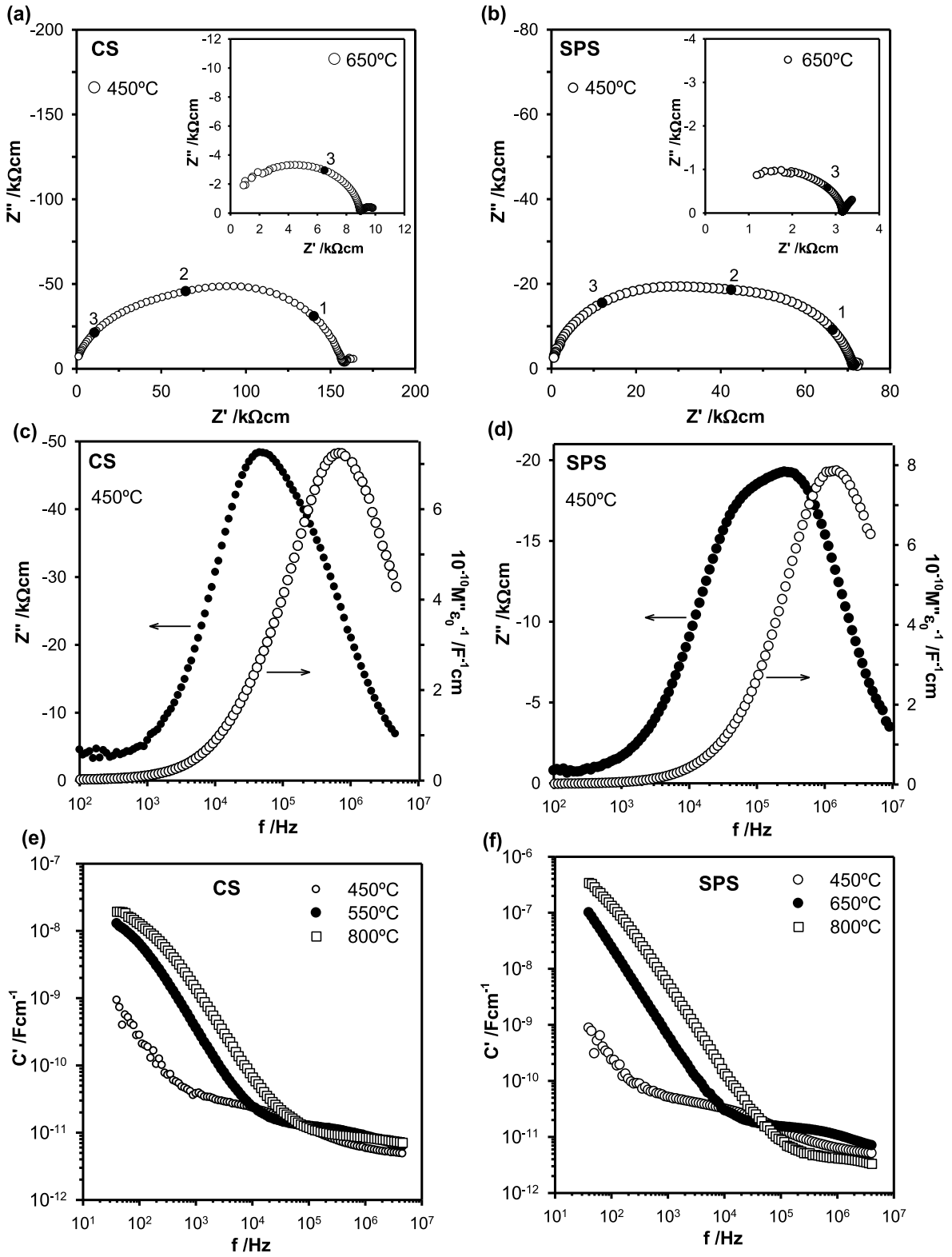

Fig. 5. Impedance complex plane plots (a–b), Z''/M'' spectroscopy plots (c–d) and log C' *vs* log f plots (e–f) at different temperatures for SZ sample. All IS measurements were performed in dry nitrogen. The solid data points and numbers in (a–b) refer to frequencies of 10 kHz (1), 100 kHz (2) and 1 MHz (3).

components were observed in both processes, associated with the bulk and the grain boundary, with capacitance values of approximately 6 x 10^{-12} F cm^{-1} for the bulk and 1.8–1.2 x 10^{-10} F cm^{-1} for the grain boundaries. The presence of these two RC components was more clearly observed in the samples with magnesium. At low frequencies, a spike in the impedance plot, which evolves into a depressed semicircle with a small resistance at high temperatures, was observed in both samples, along with an increase in C' to values ranging from approximately 10^{-7} to 10^{-6} F cm^{-1}, depending on the sintering process, indicating ion blocking at the sample–electrode interface. Therefore, electrically inhomogeneous samples were obtained in both sintering methods.

The total resistance of each sample was obtained from the intercepts

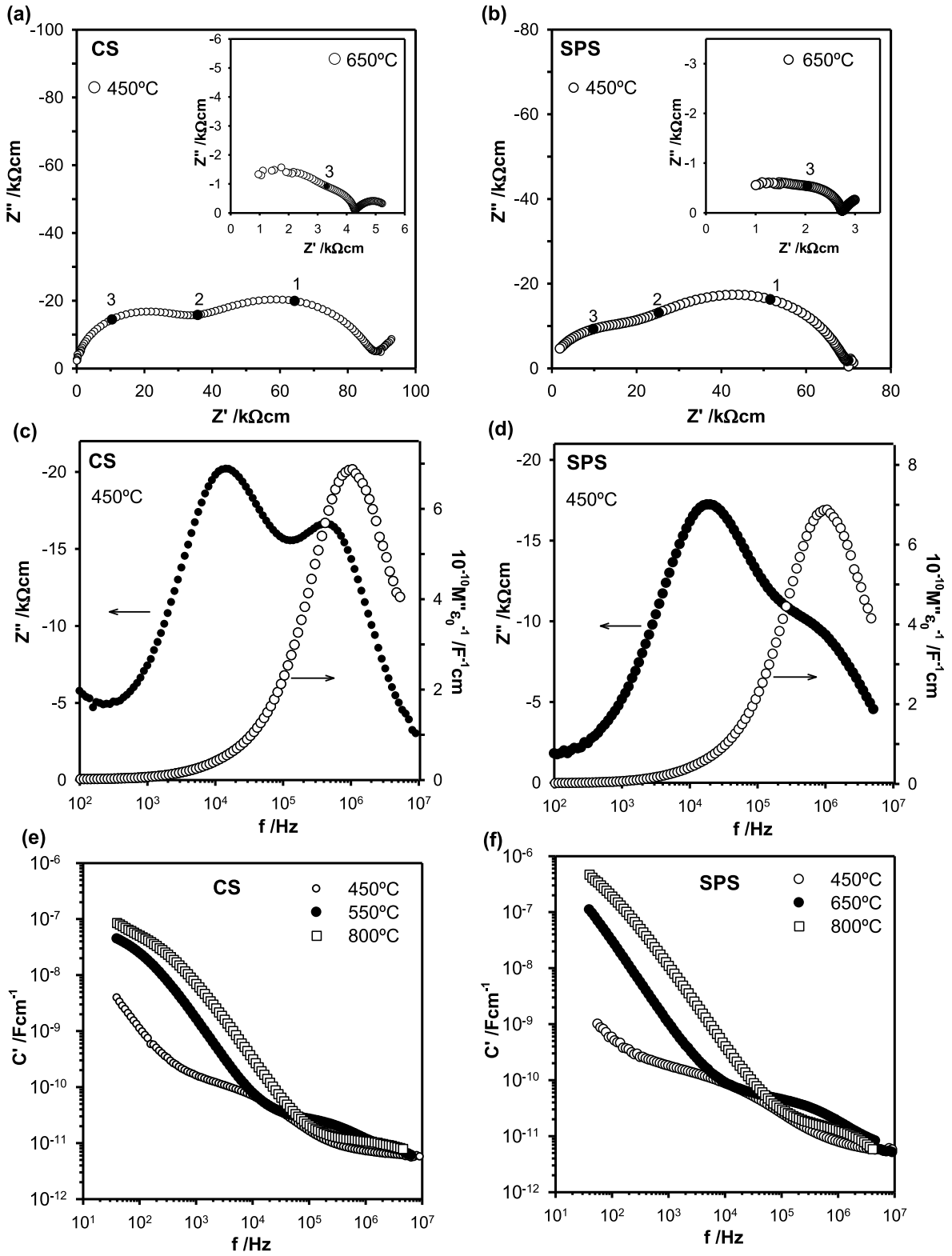

Fig. 6. Impedance complex plane plots (a–b), Z''/M'' spectroscopy plots (c–d) and log C' *vs* log f plots (e–f) at different temperatures for SZM01 sample. All IS measurements were taken in dry nitrogen. The solid data points and numbers in (a–b) refer to frequencies of 10 kHz (1), 100 kHz (2) and 1 MHz (3).

of the arc on the Z′ axis in the impedance complex plane plots. This is then presented as total conductivity in Arrhenius format as a function of temperature, as shown in Fig. S3 of the Supplementary Information. EIS measurements at different temperatures were conducted after the system reached steady-state conditions. All samples prepared by SPS exhibited similar conductivities, with SZM02 being the most resistive. In contrast, the samples prepared by CS showed slight variations in total conductivity, with sample SZM01 displaying the highest conductivity. Due to the electrical inhomogeneity observed in all samples, and to analyze the behavior in each region of the sample in detail, the conductivity data for each region, bulk (σ_1) and grain boundary (σ_2), were extracted from the impedance data shown in Fig. 5(a–d) and 6(a-d) and

represented in Arrhenius format in Fig. 7 for both sintering processes.

For the samples prepared by CS (Fig. 7a and b), the effect of doping is evident in the SZM01 sample, where conductivity increases drastically, promoting oxide-ion conductivity as Zr(IV) is substituted by Mg(II) in the pyrochlore structure. However, when the Mg concentration is higher, conductivity decreases. This behavior is similar in both regions of the sample.

For the samples prepared by SPS (Fig. 7c and d), the effect of doping is more evident in the bulk region, with the SZM01 sample showing the highest conductivity. However, similar conductivities were observed concerning the grain boundary contribution. Consequently, as the total resistance of the samples is dominated by the grain boundaries, all samples exhibit similar values in total conductivity (see Fig. S3 of the SI).

Therefore, in both sintering processes, the SZM01 sample exhibits the highest conductivity, with conductivity decreasing as the magnesium concentration increases. This behavior in the decrease of conductivity could be associated with the density of mobile charge carriers.

The activation energies and preexponential factors for all samples prepared by the two sintering processes, extracted from the Arrhenius plots in Fig. 7, are presented in Table 3. The activation energies for the bulk and grain boundary regions differ clearly, but there is no significant variation in activation energy with respect to dopant content; thus, oxygen-ion conduction remains the conduction mechanism in all cases. On the other hand, a notable increase in the pre-exponential factor is

Table 3
Activation energies and pre-exponential factor extracted from the Arrhenius plots.

		SZ	SZM01	SZM015	SZM02
Conventional sintering					
Ea/eV	σ_1	0.70	0.71	0.73	0.76
	σ_2	0.91	0.95	0.93	0.92
Pre-exponential factor/Scm^{-1}	σ_1	2.87	3.89	2.84	2.46
	σ_2	19.45	112.72	28.90	15.95
SPS					
Ea/eV	σ_1	0.72	0.72	0.70	0.69
	σ_2	1.00	1.00	0.99	0.99
Pre-exponential factor/Scm^{-1}	σ_1	4.26	13.24	7.66	5.83
	σ_2	226.4	266.6	288.6	160.7

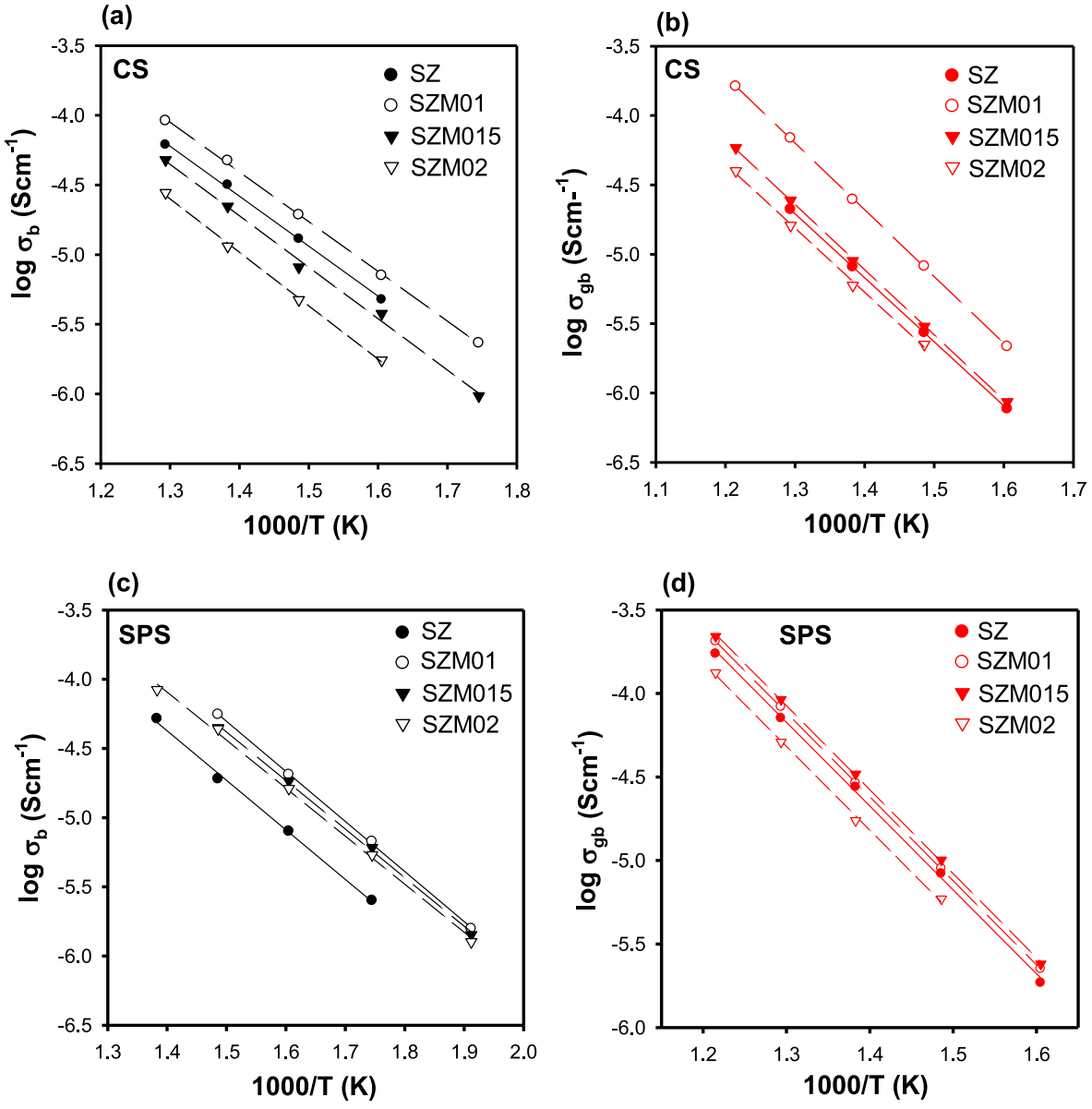

Fig. 7. Arrhenius plots of bulk (σ_b) and grain boundary (σ_{gb}) conductivity in dry N_2 for all samples prepared by the two sintering processes: (a, b) CS and (c, d) SPS.

observed with doping, with a maximum for the SZM01 sample, which also exhibits the highest conductivity. Since the preexponential factor is known to be associated with the density of mobile charge carriers, this suggests that SZM01 has a significantly higher concentration of mobile charge carriers compared to the other samples.

Since the SZM01 sample has the highest conductivity, and in order to compare it with the stoichiometric sample, SZ, a fitting of the data was performed at high and mid frequencies for these samples sintered by CS and SPS to extract accurate data for the two components and evaluate the potential blocking effect within the material. The fits of the samples are shown in Fig. S4 for measurements taken at 450 °C, and the data obtained from these fits are included in Table S1 for four different temperatures. The equivalent circuit chosen to represent the high- and medium-frequency ranges of the impedance data is also shown in Fig. S4. The proposed circuit for modelling this frequency range consists of two parallel combinations of a resistance (R) and a Constant Phase Element (CPE), connected in series. The high-frequency R_1-CPE_1 combination is attributed to the bulk, while the medium-frequency R_2-CPE_2 combination is attributed to the grain boundary. The fitting data, along with the original data and the two components extracted from the fitting, are shown in Fig. S4, demonstrating a good fit for all data.

On the other hand, Fig. 8 show the variation of the log *f*max with temperature in Arrhenius format for SZ and SZM01 samples sintered by CS and SPS. This representation serves as a powerful tool for determining the activation energy of the processes responsible for blocking charge carriers. The blocking factors, α_R, which is proportional to the blocking surface, and α_f, corresponding to the blocking thickness, can be estimated using the following equations (3) and (4):

$$\alpha_R = \frac{R_{gb}}{(R_{gb} + R_b)} \tag{3}$$

$$\alpha_f = \frac{f_{gb}}{f_b} \tag{4}$$

Therefore, the product α_R x α_f is proportional to the blocking volume in the ceramic sample. According to the EIS measurements at different temperatures, the SPS process significantly reduces the average blocking volume from 7.9 % to 4.3 % for SZ and from 1.5 % to 1.3 % for SZM01, likely due to a decrease in sample porosity.

To more clearly evaluate the conductivity of the samples prepared by both sintering processes, Fig. 9(a) and (b) show a comparison of the total conductivity of the SZ and SZM01 samples, respectively. As seen in this figure, conductivity is higher in both cases for the samples prepared by SPS. The increase in conductivity could be assigned to the higher density of the samples, which reduces the blocking effect due to the porosity.

The total conductivity curve for the SZM01 sample in a reducing atmosphere (5 % H_2/95 % N_2) showed no notable differences compared to the curves measured in nitrogen and air. This indicates that the SZM01 material remains stable, with no reduction or oxidation occurring under the conditions tested (Fig. 10(a)). This issue is a key parameter for the use of the material as electrolyte in SOFC and SOEC devices.

It is important to note that the conductivity values obtained are higher than those reported for other pyrochlore systems in the literature, such as $Gd_2Zr_2O_7$ [64], $Pr_2Zr_2O_7$ [42] or $Nd_2Zr_2O_7$ [65]. Moreover, when compared to the conductivities of $Sm_2Zr_2O_7$-based compositions reported by other authors [30,32–36,61], our samples exhibit similar values; however, it is worth highlighting that they have been processed at significantly lower sintering temperatures. Furthermore, the conductivity values for the undoped SZ sample prepared by SPS are similar to those previously reported by our group [61] at the same temperature. Therefore, the use of SPS for sintering the samples enables achieving high densities at lower temperatures and in very short times, while also yielding good conductivity values. As observed in other studies involving different materials, such as lithium-ion conducting ceramics [66,67], $ZnFe_2O_4$ for energy storage materials [68], or ceramics used in heterostructured electrodes for hydrogen energy technologies [69], the SPS process enables the production of various materials with suitable properties for different applications.

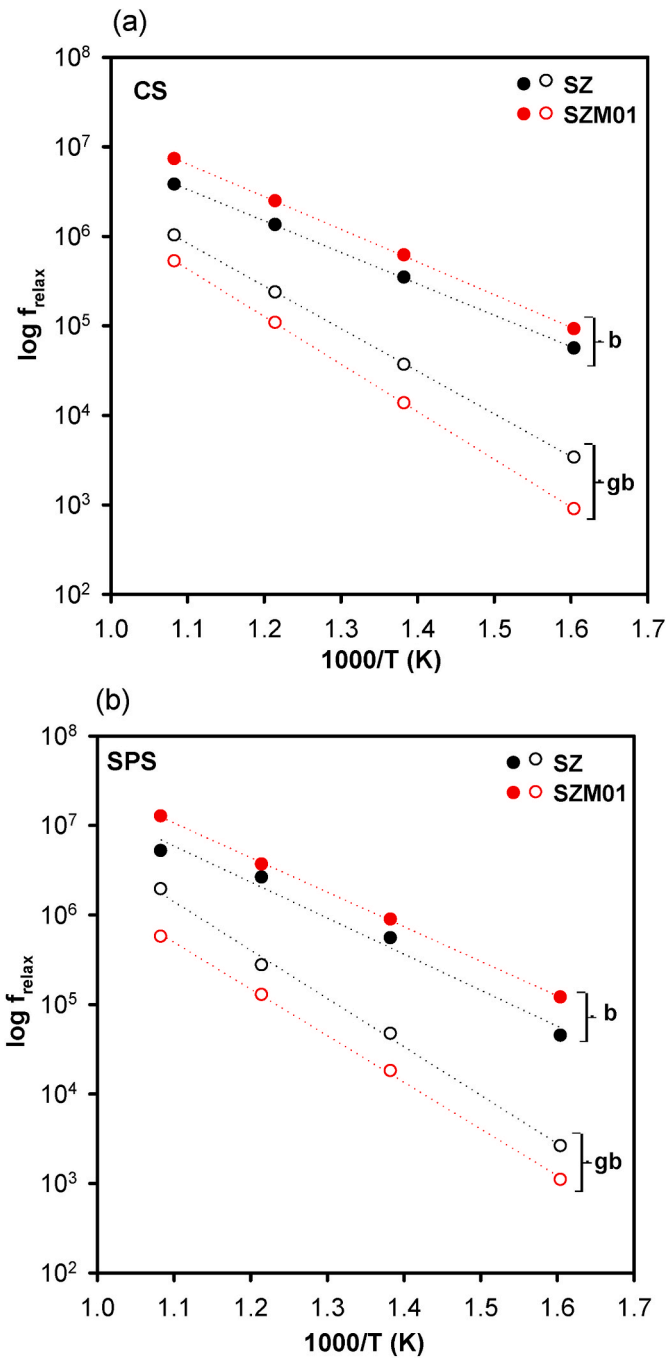

Fig. 8. Variation of the log f_{max} with temperature in Arrhenius format of bulk and grain boundary for SZ and SZM01 sintered by CS (a) and SPS (b).

Finally, since sample SZM01 exhibits the highest conductivity, Fig. 10(b) presents a comparison between this sample and a reference material commonly used as solid electrolyte for SOFCs, which also exhibit favorable characteristics such as good ionic conductivity and high-temperature stability. In this case, sample SZM01 shows conductivities similar or slightly better to YSZ [70] across the entire temperature range. As a result, this material appears to be promising for use in fuel cells and other energy-related technologies.

In summary, the samples demonstrate promising ionic transport properties, particularly those prepared by SPS, exhibiting high

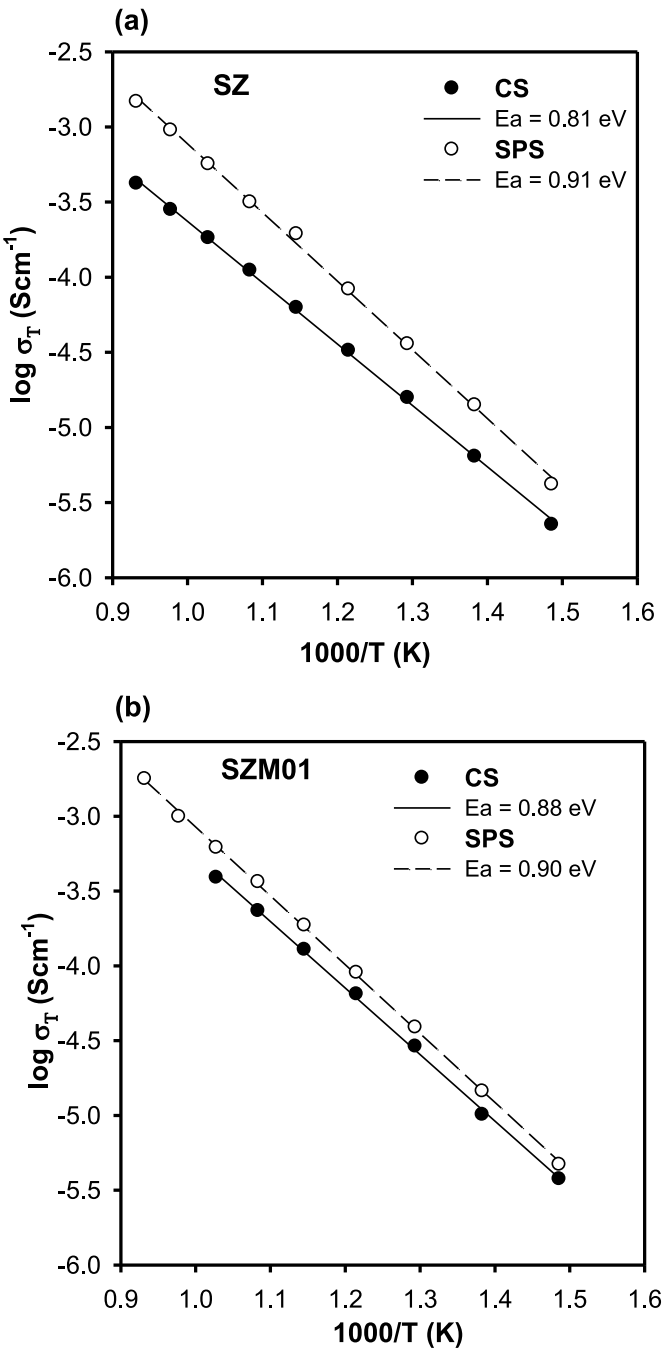

Fig. 9. Arrhenius plots of the overall conductivity in dry N_2 for the (a) SZ and (b) SZM01 samples prepared by the two sintering processes.

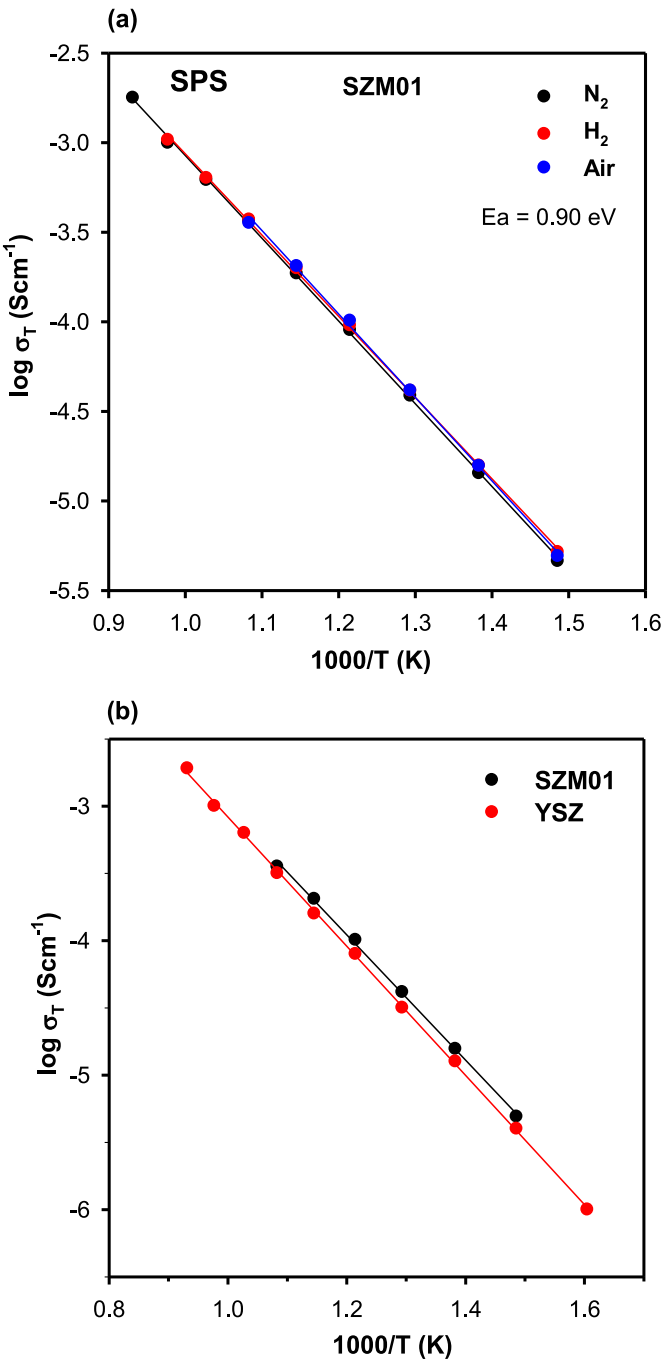

Fig. 10. Arrhenius plots of the SZM01 overall conductivity in dry N_2, air and 5 %H_2/95 %N_2 and (b) compared to referenced ion-oxide solid electrolyte material, YSZ [65], in air.

conductivity over a wide temperature range and good stability in both oxidizing and reducing atmospheres, an important characteristic for various technological applications. In particular, the SZM01 sample seems to be a promising material for a wide range of applications, including SOFCs and High Temperature Steam Electrolysers (HTSE).

4. Conclusions

Single-phase of pyrochlore materials based on $Sm_2Zr_{2-x}Mg_xO_{7-x}$ (x = 0, 0.1, 0.15 and 0.2) were synthesized using the solvothermal method at 180 °C and subsequently fired at 1200 °C for 2h. Pellets prepared through two different sintering processes, conventional sintering (CS) and Spark Plasma Sintering (SPS), at 1350 °C also exhibited single-phase of pyrochlore structure. However, the densities differed significantly: the samples prepared by CS reached approximately 70 %, while those processed by SPS achieved 97 %. These differences in relative density, and consequently in the sintering quality, were clearly observed through SEM analysis. Furthermore, a reduction in crystal size, as determined by XRD, was evident in the SPS samples, which may contribute to improved sintering.

Electrochemical Impedance spectroscopy (EIS) measurements conducted under dry nitrogen showed that the samples were electrically inhomogeneous. To describe the electrical response, two RC elements associated in series were required, with the grain boundary component dominating the overall conductivity response. The samples prepared by SPS exhibited higher ionic conductivity values than those prepared by

CS. Although Mg doping improves both grain boundary and bulk conductivity in both sintering methods, further increasing the Mg concentration does not lead to higher conductivity. The highest conductivity values were observed in the SZM01 sample.

Therefore, a correlation between microstructure for each of the processes with conductivity was clearly observed, with SPS sintering generating the highest conductivities.

A comparison with the classical ion-oxide solid electrolyte material, YSZ, sintered via SPS revealed that the SZM01 sample exhibited higher conductivity over the entire temperature range. Moreover, this composition exhibited nearly identical conductivity under nitrogen, air, and reducing (5 % H_2/95 % N_2) atmospheres, indicating that the material remains stable under the tested conditions.

Due to their outstanding relative density and high conductivity, especially in SZM01 sample prepared by SPS, these materials show great potential for use in applications that demand thermal and physical stability alongside swift oxidation-reduction capabilities. Such applications include Solid Oxide Fuel Cells (SOFCs), and Solid Oxide Electrolysis Cells (SOECs), gas sensors, and various clean energy technologies.

Data availability

The data supporting this article have been included in the text or as part of the Supplementary Information.

Declaration of competing interest

The authors declare that they have no known competing financial interests or personal relationships that could have appeared to influence the work reported in this paper.

Acknowledgments

H.B-M, E.C. and S.B-Z thank the Spanish *Ministerio de Ciencia e Innovación* for the grant PID2020-116149 GB-I00 funded by MCIN/AEI/10.13039/501100011033. S.B-Z also thanks *Universitat Jaume I* and the *Ministerio de Ciencia, Innovación y Universidades* for the FPI [PREDOC/2023/06] and FPU23/02832 predoctoral contracts. ELSV thanks the National Council for Scientific and Technological Development (CNPq process 446879/2024-0).

Appendix A. Supplementary data

Supplementary data to this article can be found online at https://doi.org/10.1016/j.jmrt.2025.07.080.

References

[1] Zhang J, Ricote S, Hendriksen PV, Chen Y. Advanced materials for thin-film solid oxide fuel cells: recent progress and challenges in boosting the device performance at low temperatures. Adv Funct Mater 2022;32:2111205. https://doi.org/10.1002/adfm.202111205.

[2] Choi JL, Park BK, Lee SB, Song RH, Lee JW. Efficient and robust ceramic interconnects based on a mixed-cation perovskite for solid oxide fuel cells. Ceram Int 2019;45:4902–8. https://doi.org/10.1016/j.ceramint.2018.11.189.

[3] Singh K, Kannan R, Thangadurai V. Perspective of perovskite-type oxides for proton conducting solid oxide fuel cells. Solid State Ionics 2019;339:114951. https://doi.org/10.1016/j.ssi.2019.04.014.

[4] Shao Z, Zhou W, Zhu Z. Advanced synthesis of materials for intermediate-temperature solid oxide fuel cells. Prog Mater Sci 2012;57:804–74. https://doi.org/10.1016/j.pmatsci.2011.08.002.

[5] Basu B, Balani K. Advanced structural ceramics. Wiley; 2011. https://doi.org/10.1002/9781118037300.

[6] Shackelford JF, Doremus RH. Ceramic and glass materials: structure, properties and processing. Springer; 2008. https://doi.org/10.1007/978-0-387-73362-3.

[7] Subramanian M, Aravamudan G, Subba Rao G. Oxide pyrochlores - a review. Prog Solid State Chem 1983;15:55–143. https://doi.org/10.1016/0079-6786(83)90001-8.

[8] Blundred GD, Bridges CA, Rosseinsky MJ. New oxidation states and defect chemistry in the pyrochlore structure. Angew Chem Int Ed 2004;43:3562–5. https://doi.org/10.1002/anie.200453819.

[9] Mouta R, Silva RX, Paschoal CWA. Tolerance factor for pyrochlores and related structures. Acta Crystallogr B: Struct Sci Cryst Eng Mater 2013;69:439–45. https://doi.org/10.1107/S2052519213020514.

[10] Mahato N, Banerjee A, Gupta A, Omar S, Balani K. Progress in material selection for solid oxide fuel cell technology: a review. Prog Mater Sci 2015;72:141–337. https://doi.org/10.1016/j.pmatsci.2015.01.001.

[11] Varcoe JR, Atanassov P, Dekel DR, Herring AM, Hickner MA, Kohl PA, Kucernak AR, Mustain WE, Nijmeijer K, Scott K, Xu T, Zhuang L. Anion-exchange membranes in electrochemical energy systems. Energy Environ Sci 2014;7:3135–91. https://doi.org/10.1039/c4ee01303d.

[12] Cioateră N, Voinea E-A, Spînu C-I. Pyrochlores as cathodes in solid oxide fuel cells. Opt Mater X 2022;24:433–48. https://doi.org/10.1016/B978-0-323-90483-4.00013-1.

[13] Shlyakhtina AV, Pigalskiy KS. Tolerance factor as the basic criterion in searching for promising oxygen-ion and proton conductors among $Ln_{2-x}D_xM_2O_{7-\delta}$ (Ln = La-Lu; M= Sn, Ti, Zr, Hf; D= Sr, Ca, Mg; x = 0, 0.1) 3+/4+ pyrochlores. Mater Res Bull 2019;116:72–8. https://doi.org/10.1016/j.materresbull.2019.04.021.

[14] Jiang L, Liu Y, Sun W, Tang M, Zhang Y, Lv S, Wang J, Liu Y, Wang C, Sun P, Zheng J, Liu F, Lu G. Mixed potential type sensor based on $Gd_2Zr_2O_7$ solid electrolyte and $BiVO_4$ sensing electrode for effective detection of triethylamine. J Hazard Mater 2022;440:129695. https://doi.org/10.1016/j.jhazmat.2022.129695. 2022.

[15] Ganesan M, Jayaraman V, Selvaraj P, Mani KM, Kim DH. Pyrochlore cerium stannate ($Ce_2Sn_2O_7$) for highly sensitive NO_2 gas sensing at room temperature. Appl Surf Sci 2023;624:157135. https://doi.org/10.1016/j.apsusc.2023.157135.

[16] Jiang L, Wang C, Wang J, Liu F, You R, Lv S, Zeng G, Yang Z, He J, Liu A, Yan X, Sun P, Zheng J, Lu G. Pyrochlore Ca-doped $Gd_2Zr_2O_7$ solid state electrolyte type sensor coupled with ZnO sensing electrode for sensitive detection of HCHO. Sensor Actuator B Chem 2020;309:127768. https://doi.org/10.1016/j.snb.2020.127768.

[17] Kuznetsov DA, Naeem MA, Kumar PV, Abdala PM, Fedorov A, Müller CR. Tailoring lattice oxygen binding in ruthenium pyrochlores to enhance oxygen evolution activity. J Am Chem Soc 2020;142:7883–8. https://doi.org/10.1021/jacs.0c01135.

[18] Sun S, Xue Y, Yang D, Pei Z, Fang L, Xia Y, Ti R, Wang C, Liu C, Xiong B, Fu Z, Yin X. Bismuth pyrochlores with varying Fe/Co ratio for efficient Multi-functional Catalysis: structure evolution versus Photo- and Electro-catalytic activities. Chem Eng J 2022;448:137580. https://doi.org/10.1016/j.cej.2022.137580.

[19] Jain D, Saha S. Spectroscopic and kinetic insights into the methane reforming over Ce-pyrochlores. Mol Catal 2020;492:110964. https://doi.org/10.1016/j.mcat.2020.110964.

[20] Deng J, Li S, Yin X, Li M, Wang J, Chen Y, Chen Y. Influence of surface Ce/Zr ratio on formation of κ-$Ce_2Zr_2O_8$ superstructure and its application in three-way catalysis. J Rare Earths 2023;41:67–76. https://doi.org/10.1016/j.jre.2021.12.005.

[21] dos Santos Veiga EL, Villafruela XV, Llorca J, Beltrán-Mir H, Cordoncillo E. The catalytic activity of the $Pr_2Zr_{2-x}Fe_xO_{7\pm\delta}$ system for the CO oxidation reaction. J Am Ceram Soc 2023;106:1369–80. https://doi.org/10.1111/jace.18846.

[22] dos Santos Veiga EL, Díaz-Verde Á, Illán-Gómez MJ, Beltrán-Mir H, Cordoncillo E. Evaluation of $Pr_2Zr_{2-x}Ce_xO_{7\pm\delta}$ pyrochlores as a potential Cu support catalysts for CO oxidation in simulated GDI conditions. Appl Catal B Environ 2024;342:123371. https://doi.org/10.1016/j.apcatb.2023.123371.

[23] Lan G, Ouyang B, Song J. The role of low-lying optical phonons in lattice thermal conductance of rare-earth pyrochlores: a first-principle study. Acta Mater 2015;91:304–17. https://doi.org/10.1016/j.actamat.2015.03.004.

[24] Fan Y, Wu Q, Yao Y, Wang J, Zhao J, Liu B. Temperature effect on mechanical and thermal properties of multicomponent rare-earth zirconate pyrochlores. J Am Ceram Soc 2023;106:1500–12. https://doi.org/10.1111/jace.18816.

[25] Gao L, Liang K, Guan Z, Liu Z, Fang Z, Chen H, Zhang J. Disordered structures and dielectric properties of Ni-doped bismuth magnesium niobate pyrochlores. J Phys Chem C 2021;125:27793–9. https://doi.org/10.1021/acs.jpcc.1c08515.

[26] Liang K, Gao L, Fang Z, Liu Z, Guan Z, Chen H, Zhang J. Effects of Ni^{2+} substitution on the structure and dielectric properties of $Bi_{1.5}MgNb_{1.5}O_7$ cubic pyrochlores. J Eur Ceram Soc 2021;41:3425–31. https://doi.org/10.1016/j.jeurceramsoc.2020.10.030.

[27] Díaz-Guillén JA, Fuentes AF, Díaz-Guillén MR, Almanza JM, Santamaría J, León C. The effect of homovalent A-site substitutions on the ionic conductivity of pyrochlore-type $Gd_2Zr_2O_7$. J Power Sources 2009;186:349–52. https://doi.org/10.1016/j.jpowsour.2008.09.106.

[28] Shlyakhtina AV, Savvin SN, Levchenko AV, Knotko AV, Fedtke P, Busch A, Barfels T, Wienecke M, Shcherbakova LG. Study of bulk and grain-boundary conductivity of $Ln_{2+x}Hf_{2-x}O_{7-\delta}$ (Ln = Sm-Gd; x = 0, 0.096) pyrochlores. J Electroceram 2010;24:300–7. https://doi.org/10.1007/s10832-009-9572-0.

[29] Gill JK, Pandey OP, Singh K. Ionic conductivity, structural and thermal properties of pure and Sr^{2+} doped $Y_2Ti_2O_7$ pyrochlores for SOFC. Solid State Sci 2011;13:1960–6. https://doi.org/10.1016/j.solidstatesciences.2011.08.025.

[30] Shlyakhtina AV, Knotko AV, Boguslavskii MV, Stefanovich SY, Kolbanev IV, Larina LL, Shcherbakova LG. Effect of non-stoichiometry and synthesis temperature on the structure and conductivity of $Ln_{2+x}M_{2-x}O_{7-x/2}$ (Ln = Sm-Gd; M = Zr, Hf; x = 0-0.286). Solid State Ionics 2007;178:59–66. https://doi.org/10.1016/j.ssi.2006.11.001.

[31] Zhang HS, Li ZJ, Xu Q, Wang FC, Liu L. Preparation and thermophysical properties of $Sm_2(Ce_{0.3}Zr_{0.7})_2O_7$ ceramic. Adv Eng Mater 2008;10:139–42. https://doi.org/10.1002/adem.200700153.

[32] Xia XL, Ouyang JH, Liu ZG. Influence of CaO on structure and electrical conductivity of pyrochlore-type $Sm_2Zr_2O_7$. J Power Sources 2009;189:888–93. https://doi.org/10.1016/j.jpowsour.2008.12.136.

[33] Liu ZG, Ouyang JH, Zhou Y, Xiang J, Liu XM. Preparation, structure and electrical conductivity of pyrochlore-type samarium-lanthanum zirconate ceramics. Mater Des 2011;32:4201–6. https://doi.org/10.1016/j.matdes.2011.04.036.

[34] Liu ZG, Ouyang JH, Sun KN, Zhou Y. Electrical conductivity of 5 mol.% Yb_2O_3 and 5 mol.% Gd_2O_3 co-doped $Sm_2Zr_2O_7$. Mater Lett 2011;65:385–7. https://doi.org/10.1016/j.matlet.2010.10.032.

[35] Xia XL, Liu ZG, Ouyang JH, Zheng Y. Preparation, structural characterization, and enhanced electrical conductivity of pyrochlore-type $(Sm_{1-x}Eu_x)_2Zr_2O_7$ ceramics. Fuel Cells 2012;12:624–32. https://doi.org/10.1002/fuce.201200015.

[36] Vaisakhan Thampi DS, Prabhakar Rao P, Radhakrishnan AN. Influence of Ce substitution on the order-to-disorder structural transition, thermal expansion and electrical properties in $Sm_2Zr_{2-x}Ce_xO_7$ system. RSC Adv 2014;4:12321–9. https://doi.org/10.1039/c3ra47001f.

[37] Ma YH, Liu ZG, Ouyang JH, Jin YJ. Influence of TiO_2 doping on thermo-optical properties of pyrochlore $Sm_2(Zr_{1-x}Ti_x)_2O_7$ ($0 \leq x \leq 0.15$) ceramics. Ceram Int 2016;42:14749–53. https://doi.org/10.1016/j.ceramint.2016.06.102.

[38] Wang DY, Liu L, Liu YB, Li T, Ma Z, Wu HX. Heat insulating capacity of $Sm_2Zr_2O_7$ coating added with high absorptivity solids. Ceram Int 2017;43:2884–7. https://doi.org/10.1016/j.ceramint.2016.11.068.

[39] Guo W, Ma Z, Liu L, Liu Y. Influence of feedstock on the microstructure of $Sm_2Zr_2O_7$ thermal barrier coatings deposited by plasma spraying. J Therm Spray Technol 2018;27:1524–31. https://doi.org/10.1007/s11666-018-0803-2.

[40] Shlyakhtina AV, Abrantes JCC, Gomes E, Lyskov NV, Konysheva EY, Chernyak SA, Kharitonova EP, Karyagina OK, Kolbanev IV, Shcherbakova LG. Evolution of oxygen-ion and proton conductivity in Ca-doped $Ln_2Zr_2O_7$ (Ln = Sm, Gd), located near pyrochlore-fluorite phase boundary. Materials 2019;12:2452. https://doi.org/10.3390/ma12152452.

[41] Zheng Y, Duan P, Li Z, Cai G, Zhong F, Xiao Y. Heterovalent ions incorporated pyrochlore $Sm_2Zr_2O_7$ ceramic for enhanced NO_2 sensing. J Eur Ceram Soc 2020;40:3453–61. https://doi.org/10.1016/j.jeurceramsoc.2020.03.042.

[42] dos Santos-Veiga EL, Fortuño-Morte M, Beltrán-Mir H, Cordoncillo E. Effect of the oxidation states on the electrical properties of Fe-doped $Pr_2Zr_2O_7$ pyrochlore. J Mater Res Technol 2022;16:201–15. https://doi.org/10.1016/j.jmrt.2021.11.146.

[43] Cologna M, Rashkova B, Raj R. Flash sintering of nanograin zirconia in <5 s at 850°C. J Am Ceram Soc 2010;93:3556–9. https://doi.org/10.1111/j.1551-2916.2010.04089.x.

[44] Guo H, Baker A, Guo J, Randall CA. Cold sintering process: a novel technique for low-temperature ceramic processing of ferroelectrics. J Am Ceram Soc 2016;99:3489–507. https://doi.org/10.1111/jace.14554.

[45] Munir ZA, Anselmi-Tamburini U, Ohyanagi M. The effect of electric field and pressure on the synthesis and consolidation of materials: a review of the spark plasma sintering method. J Mater Sci 2006;41:763–77. https://doi.org/10.1007/s10853-006-6555-2.

[46] Legallais M, Fourcade S, Chung UC, Michau D, Maglione M, Mauvy F, Elissalde C. Fast re-oxidation kinetics and conduction pathway in Spark Plasma Sintered ferroelectric ceramics. J Eur Ceram Soc 2018;38:543–50. https://doi.org/10.1016/j.jeurceramsoc.2017.07.026.

[47] Zhang ZH, Liu ZF, Lu JF, Shen XB, Wang FC, Wang YD. The sintering mechanism in spark plasma sintering - proof of the occurrence of spark discharge. Scr Mater 2014;81:56–9. https://doi.org/10.1016/j.scriptamat.2014.03.011.

[48] B.N. Ezealigo, R. Orrù, C. Elissalde, H. Debéda, U.-C. Chung, M. Maglione, G. Cao, Influence of the Spark Plasma Sintering temperature on the structure and dielèctric properties of $BaTi_{(1-x)}Zr_xO_3$ ceramics, Ceram Int 2021 (n.d.) 3614–3625. https://doi.org/10.1016/j.ceramint.2020.09.210.

[49] Liu B, Zhang Y. $La_{0.9}Sr_{0.1}Ga_{0.8}Mg_{0.2}O_{3-\delta}$ sintered by spark plasma sintering (SPS) for intermediate temperature SOFC electrolyte. J Alloys Compd 2008;458:383–9. https://doi.org/10.1016/j.jallcom.2007.03.126.

[50] Blake GR, Hartge KH. Bulk density. In: Klute A, editor. Methods of soil analysis: Part 1 physical and mineralogical methods. American Society of Agronomy; 1986. p. 363–75. https://doi.org/10.2136/sssabookser5.1.2ed.c13.

[51] Anantharaman AP, Dasari HP. Potential of pyrochlore structure materials in solid oxide fuel cell applications. Ceram Int 2021;47:4367–88. https://doi.org/10.1016/j.ceramint.2020.10.012.

[52] Mandal BP, Garg N, Sharma SM, Tyagi AK. Preparation, XRD and Raman spectroscopic studies on new compounds $RE_2Hf_2O_7$ (RE=Dy, Ho, Er, Tm, Lu, Y): pyrochlores or defect-fluorite? J Solid State Chem 2006;179:1990–4. https://doi.org/10.1016/j.jssc.2006.03.036.

[53] Shannon RD. Revised effective ionic radii and systematic studies of interatomic distances in halides and chalcogenides. Acta Crystallogr A 1976;32:751–67. https://doi.org/10.1107/S0567739476001551.

[54] West AR. Solid state chemistry and its applications. Wiley; 2022.

[55] Qu Z, Wan C, Pan W. Thermal expansion and defect chemistry of MgO-doped $Sm_2Zr_2O_7$. Chem Mater 2007;19:4913–8. https://doi.org/10.1021/cm071615z.

[56] Zhang S, Xu J, Lu C, Ouyang R, Ma J, Zhong X, Fang X, Xu X, Wang X. Preparation method investigation and structure identification by XRD and Raman techniques for $A_2B_2O_7$ composite oxides. J Am Ceram Soc 2024;107:3475–96. https://doi.org/10.1111/jace.19645.

[57] Scheetz BE, White WB. Characterization of anion disorder in zirconate $A_2B_2O_7$ compounds by Raman spectroscopy. J Am Ceram Soc 1979;62:468–70. https://doi.org/10.1111/j.1151-2916.1979.tb19107.x.

[58] Ghayoor R, Yousefi MH. Spark plasma sintered YSZ gas electrode produced from powders synthesized by a large-scale method. Mater Chem Phys 2022;289:126467. https://doi.org/10.1016/j.matchemphys.2022.126467.

[59] Chen XJ, Khor KA, Chan SH, Yu LG. Preparation yttria-stabilized zirconia electrolyte by spark-plasma sintering. Mater Sci Eng 2003;341:43–8. https://doi.org/10.1016/S0921-5093(02)00079-5.

[60] Adler SB. Factors governing oxygen reduction in solid oxide fuel cell cathodes. Chem Rev 2004;104:4791–843. https://doi.org/10.1021/cr020724o.

[61] dos Santos Veiga EL, Beltrán-Mir H, Fourcade S, Chung UC, Michau D, Elissalde C, Mauvy F, Cordoncillo E. Understanding the rapid reoxidation process and the electrical properties of Spark Plasma sintered pyrochlores. J Eur Ceram Soc 2024;44:4130–40. https://doi.org/10.1016/j.jeurceramsoc.2023.12.070.

[62] Irvine JTS, Sinclair DC, West AR. Electroceramics: characterization by impedance spectroscopy. Adv Mater 1990;2:132–8. https://doi.org/10.1002/adma.19900020304.

[63] Vendrell X, West AR. Electrical properties of yttria-stabilized zirconia, YSZ single crystal: local AC and long range DC conduction. J Electrochem Soc 2018;165:F966–75. https://doi.org/10.1149/2.0881811jes.

[64] Feighery AJ, Irvine JTS, Zheng C. High oxide ion conductivity in non-stoichiometric pyrochlores and fluorites in the ternary system ZrO_2-Gd_20_3-TiO. Ionics 1997;3:30–5.

[65] Vendrell X, Santos-Veiga EL, Beltrán-Mir H, Cordoncillo E, Mestres L. Induced p-type semiconductivity in Mg-doped $Nd_2Zr_2O_7$ pyrochlore system. J Eur Ceram Soc 2023;43:6967–73. https://doi.org/10.1016/j.jeurceramsoc.2023.07.061.

[66] Kunshina GB, Bocharova IV, Belov AA, Shichalin OO, Papynov EK. Consolidation of Al and Ta-substituted $Li_7La_3Zr_2O_{12}$ powders with lithium-ionic conduction by spark plasma sintering. Russ J Electrochem 2024;60:1262–70. https://doi.org/10.1134/S1023193524601499.

[67] Kunshina GB, Shichalin OO, Belov AA, Papynov EK, Bocharova IV, Shcherbin OB. Properties of $Li_{1.3}Al_{0.3}Ti_{1.7}(PO_4)_3$ lithium-conducting ceramics synthesized by spark plasma sintering. Russ J Electrochem 2023;59:173–81. https://doi.org/10.1134/S1023193523030060.

[68] Shichalin OO, Ivanov NP, Seroshtan AI, Nadaraia KV, Simonenko TL, Rogachev KA, Marmaza PA, Zaikova AR, Sin'kova MA, Ikhtonov GV, Pogodaev AV, Kolodeznikov ES, Yu Mayorov V, Shchitovskay EV, Ognev AV, Samardak AS, Yun Shi, Yu Buravlev I, Papynov EK. $ZnFe_2O_4$ controlled synthesis: key to improving properties of funcional ceramic materials for energy storage Applications. J Phys Chem Solid 2025;205:112804. https://doi.org/10.1016/j.jpcs.2025.112804.

[69] Buravlev I Yu, Vornovskikh AA, Shichalin OO, Lembikov AO, Simonenko TL, Seroshtan AI, Buravleva AA, Belov AA, Yu Kosyanov D, Papynov EK. Reactive spark plasma synthesis of Mo_2C/Mo_3Co_3C ceramic for heterostructured electrodes used for hydrogen energy Technology. Ceram Int 2024;50:14445–57. https://doi.org/10.1016/j.ceramint.2024.01.357.

[70] Bezdorozhev O, Borodianska H, Sakka Y, Vasylkiv O. Spark plasma sintered Ni-YSZ/YSZ Bi-layers for solid oxide fuel cell. J Nanosci Nanotechnol 2013;13:4150–7. https://doi.org/10.1166/jnn.2013.7213.